

Multiphysics and comparative analysis on failure detection in planetary gears

Safa Boudhraa^{1,2}, Alfonso Fernandez del Rincon¹,
Fakher Chaari², Mohamed Amine Ben Souf² ,
Mohamed Haddar² and Fernando Viadero¹

Proc IMechE Part C:
J Mechanical Engineering Science
1–14
© IMechE 2023
Article reuse guidelines:
sagepub.com/journals-permissions
DOI: 10.1177/09544062231207147
journals.sagepub.com/home/pic


Abstract

Gearbox monitoring is considered an important scientific focus for predicting preventative maintenance plans. In these systems, mechanical defects such as loading problems, eccentricity and torsional vibrations lead to shaft fatigue and other damage to various other mechanical components. Various methods have been developed to detect and identify the presence of defects in gearboxes. In this paper, we investigate the effect of gearbox faults on the current signal by defining an analytical correlation between the physical presence of the fault and the stator current. The theoretical development is supported by experimental measurements taken on a back-to-back planetary gearbox. Planetary gearbox faults result in the motor's input torque oscillations, generating amplitude and frequency modulation (AM-FM). These modulations have an effect on stator current signals. The study of the stator current was followed by that of vibration signal and acoustic pressure taken simultaneously under the same operating conditions. This comparative investigation aims to present the differences between different techniques and highlight the efficiency of each.

Keywords

Gearbox monitoring, planetary gearbox, motor current signature, multiphysics, planet pitting

Date received: 3 January 2023; accepted: 23 September 2023

Introduction

Since gearboxes are crucial for powering various mechanical systems, monitoring them is crucial for ensuring performance and effectiveness. As a result of their crucial function, condition monitoring of these mechanisms has been ongoing and involves the status of many physical phenomena. To reduce the high costs of production stops followed by mounting, dismounting, and corrective maintenance, researchers have focused on experimental testing while building numerical models to give tools to identify any abnormality, pinpoint it, and, in general, to avoid anomalies. Vibration analysis has been the preeminent technique for checking the condition of rotating machinery under various operating situations for the past 20 years.^{1–4}

Many researchers have focused on planetary gear (PG) modeling, such as Al-Shyyab and Kahraman⁵ who have presented a non-linear dynamic model for a planetary gear set. Inalpolat and Kahraman⁶ developed a model to investigate modulation sidebands seen in the frequency spectrum. These results are validated by experimental measurements. On the other hand, Zimroz and Bartkowiak⁷ have developed a

brand-new diagnostic capability for tracking planetary gearboxes under various external stress scenarios. Vibration analysis was extensively used to investigate gears in different conditions and in for defect detection. However, measuring vibration signals inside the gearbox is impossible in some cases or very difficult because of the inaccessibility constraints in mounting the sensors.⁸ Therefore, scientific innovations are nowadays oriented toward different sophisticated techniques such as Motor Current Signature Analysis (MCSA), Acoustic Emission (AE) and Acoustic Pressure (AP). Many studies have explored the relationship between the dynamic behavior of gear sets and the motor's electrical response. The purpose of

¹Department of Structural and Mechanical Engineering, Faculty of Industrial and Telecommunications Engineering, University of Cantabria, Santander, Spain

²Laboratory of Mechanics, Modelling and Production (LA2MP), National School of Engineers of Sfax, University of Sfax, Sfax, Tunisia

Corresponding author:

Mohamed Amine Ben Souf, Laboratory of Mechanics, Modelling and Production (LA2MP), National School of Engineers of Sfax, University of Sfax, BPI 173, Sfax 3038, Tunisia.

Email: Mohamed-amine.bensouf@enis.tn

these research is to study the relationship between the electromagnetic effect in motors and the inherent vibration characteristics of the gearbox,⁹ as well as how to monitor the mechanical system using electric inputs. The MCSA was also utilized to detect mechanical imbalance in any component of the motor, as demonstrated in the work of Balan et al.,¹⁰ Feki et al.,¹¹ and Ottewill et al.¹² Within the same context, Kia et al.^{13,14} justified the presence of the gear mesh frequency components in the torque spectrum by the torsional vibrations induced by transmission error in gear pairs. These observations were followed by analytical studies that reported the vibration's impact on the current signals. In this context, Zhou et al. have worked on studying the impact of a wheel flat on the current signal in a traction motor.¹⁵ Identifying the defect was related to the frequency of the flat wheel and the gear. The associated frequency facilitates tracking, in general, any rotary component defect by means of a current signal.

In fact, the stator current is multi-component phase-modulated. In recent research, Goa et al.¹⁶ have highlighted the efficiency of the Motor current signature analysis in localizing planetary gear defects. Gear failures are represented in the current signal by sidebands around the permanent magnet synchronous generators, producing frequencies with a spacing equal to the gear fault characteristic frequencies using the Fourier spectrum. The modulation index value determines the amplitude of each gearbox-related frequency component in the stator current spectrum. Other studies discovered that the spinning frequencies associated with the motor may be clearly detected in the current spectrum at various amplitudes. However, observing the components related to mesh frequency is still critical due to its low-level energy. The presence of these components in the stator current is mainly due to the mesh frequency of the vibration transmitted to the mechanical torque.^{17,18}

Yet, less attention was given to the use of acoustic pressure as a condition monitoring indicator because of the noisy environment, which can disturb the identification of components related to the main gear defect frequencies in gears.^{19,20} Therefore, efficient isolation of the system from any external source of noise is extremely required to distinguish different sources of vibration. Some researchers worked on correlating different techniques, such as acoustic pressure, vibration signals, and current signatures to investigate the gearbox's behavior and detect the presence of any gear's fault. For planetary gears, research activities were mainly focused on studying the impact of the gear's geometric defects on vibration signals.²¹ Safa²² also, initiated the study of the impact of the gear defects on motor current and compared it to vibration signals recorded simultaneously.

This paper aims mainly to compare the capabilities of the vibration signal, current signature, and the

acoustic pressure to describe the behavior of a back-to-back planetary gearbox using an experimental-based approach. The work is structured as follows: Section 2 describes the experimental setup, composed of a two-stage planetary gearbox driven by an asynchronous motor. Also, this section presents a deep overview of all the sensors used and their locations on the test bench. We present two gear defects: one crack implemented on one of the three planets and a pitting defined on the sun.

In section 3, an analytical analysis explains the impact of vibrations resulting from mechanical systems on the driving machine. In section 4, various experimental observations in both the time and frequency domains are presented using the Fast Fourier Transform. In this section, we will establish a comparison between results to discuss the accuracy of each technique in describing the dynamic response of the gear's system, especially in the presence of defects. Finally, section 5 states conclusions from the results obtained in this paper and proposes future works.

The experimental test bench

The experimental rig

The experimental investigation work reported in this paper is done on a test rig, shown in Figure 1. It is divided into two components, the features of which are shown in Table 1. A three-phase asynchronous motor is controlled by a Siemens inverter. The mechanical part is designed as a back-to-back planetary gearbox, which is made up of two identical planetary gearbox stages (reaction and test).

Figure 1 presents different parts, which are made up of an exterior ring, three planets mounted on a carrier 1, and a sun that serves as the input gear. Back-to-back design provides mechanical power circulation for energy efficiency. Both gearboxes are linked by a stiff hollow shaft that carries both carriers and a second one that links the response gearbox's sun to the test sun.^{22,23} Reaction gear refers to the first planetary gear set, which has a fixed ring, and test gear, which has a free ring. The reaction gearbox is connected to an arm to allow adding the external load.

Instrumentations

This study involves different physical parameters. In order to ensure multidomain investigations of the test bench, current signals, acoustic pressure signals, and vibration signals will be recorded. Figure 2 illustrates the disposition of each sensor on the test bench. To measure the phase current, clamp meters of type Fluke i200s AC with 10 mA/V sensitivity were attached to the motor's input. A tri-axial accelerometer with a sensitivity of 127.02 mV/g is also mounted on the test ring to capture the system's vibration signal. Simultaneously, an optic tachometer

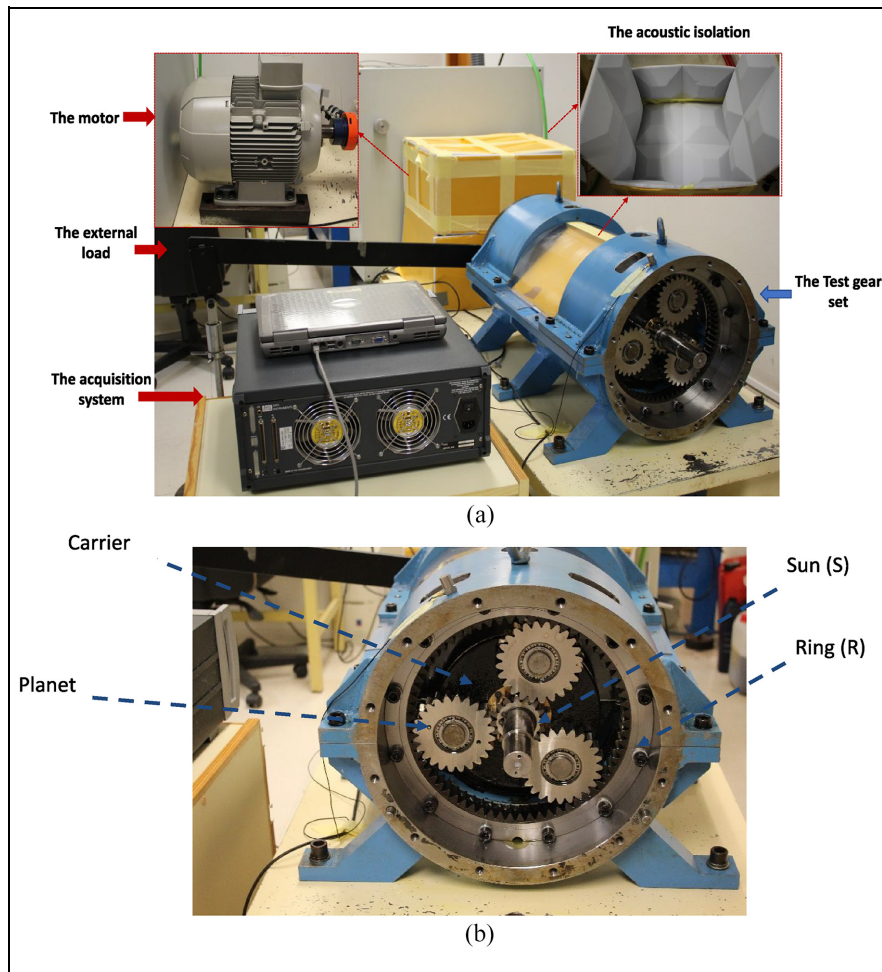


Figure 1. The experimental set-up: (a) the test bench and (b) the gearbox.

Table 1. The experimental test bench parameters.

Component					
The motor	Operating configuration				
	Frequency (Hz)	Power	Connection	Speed (rpm)	Poles
	50	15 kW	Triangle connected	1460	4
The gearbox	Component				
		Carrier	Planet	Ring	Sun
	Number	1	3	1	1
	Teeth number	–	24	65	16
	Mass (kg)	3.65	1.22	28.1	0.49

of type Compact VLS7 with pulse tapes was installed on the shaft connecting the motor to the gearbox to monitor the input shaft's angular velocity. Finally, to record the acoustic pressure of the system two microphones with 0.16 mV/Pa sensitivity each, were placed near the test gearbox. For the system isolation sheets of 10 mm were used to isolate the motor and the gearboxes.

For the data collection, all the sensors were connected to an LMS SCADAS316 monitored by LMS Test Lab software.

Key frequencies

For planetary gears, the transmission ratio depends on the fixed gear. In our case, the ring is held fixed ($\omega_r = 0$), the sun is the input of the system, and the carrier is the output. The transmission ratio R_{sc} , when the ring is held fixed,²⁴ is defined by:

$$R_{sc} = \frac{N_s}{N_c} = \frac{Z_s + Z_r}{Z_s}$$

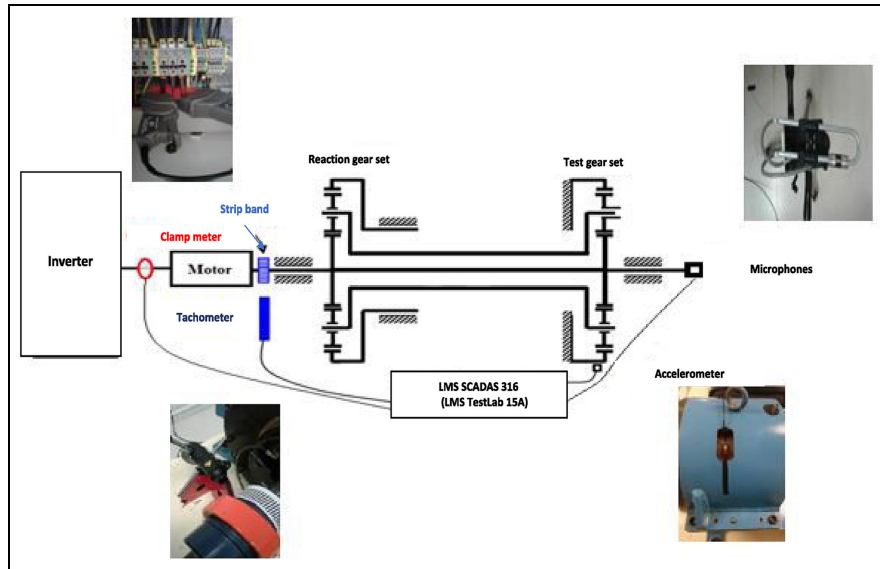


Figure 2. Instrumentations.

Table 2. Key frequencies.

Frequencies	Expression	Value (Hz)
Supply frequency	—	50
Sun frequency F_s	$F_s = \frac{N}{60}$	24.4
Carrier frequency F_c	$F_c = \frac{F_s}{R_{sc}}$	4.82
Planet passing F_{pp}	$F_{pp} = 3 F_c$	14.46
Planet frequency F_p	$F_p = 2R_{sp}F_s$	73.2
Sun frequency with respect to the carrier F_{sc}	$F_{sc} = F_s - F_c$	19.58
planet frequency with respect to the carrier F_{pc}	$F_{pc} = \frac{F_{sc}}{R_{sp}}$	13.05
Mesh frequency F_{gm}	$F_{gm} = Z_r F_c$	320.3

In the same context, the sun-planet gear ratio, which is given by: $R_{sp} = \frac{N_s}{N_p} = \frac{Z_p}{Z_s}$

where; N_i is the rotational speed (rpm) of the i th gear. Table 2 illustrates the key frequencies that characterize each rotating part of the system.

Gears defects

Electro-erosion was used to create the defects investigated in these tests. As seen in Figure 3, a pitting is also introduced on the planet's root. The cut was made along the length of the tooth, with a depth and breadth of 2 and 5 mm, respectively. In the case of the solar fault shown in Figure 3(b), a 3 mm-deep fracture was introduced.

The electromechanical impact of the dynamic behavior on the current signature

Before getting involved in studying the impact of the planetary gearboxes dynamics on the current signal,

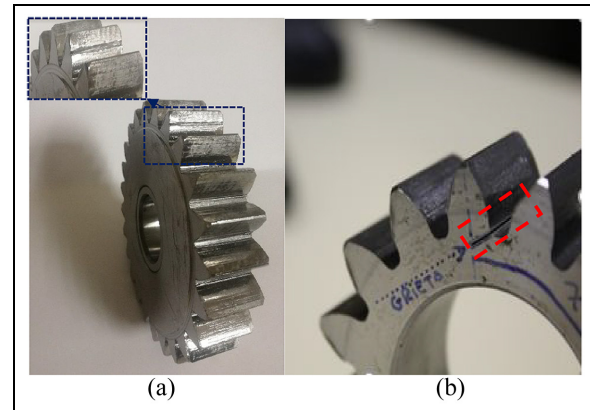


Figure 3. The teeth defect introduced on the gears: (a) a pitting on the planet and (b) a crack on the sun.

an explanation of the physical origin of the propagation of the vibrations generated by the mechanical system to the driven part is presented.

In fact, torque oscillation causes the interaction between the motor and the mechanical system. It has been demonstrated that the rotation and mesh frequency components are added to the torque signal as a result of torsional vibrations caused by load oscillations in the output gears and stiffness fluctuations caused by variation in the number of tooth pairs in contact.²⁵ The magnetomotive force MMF and permeance wave technique are used to investigate the effect of a periodic load torque fluctuation on current.²⁶ The load fluctuation is mainly due to the mechanical contact and especially to geometry defects. In the presence of external perturbation, the load variation is given as:

$$T_{load}(t) = T_c + T_{per} \cos(\omega_{per}t) \quad (1)$$

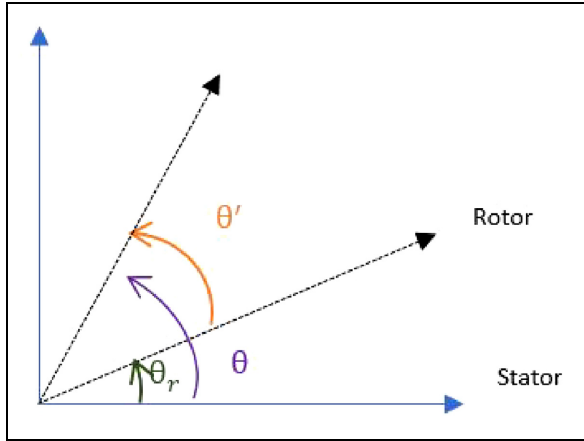


Figure 4. Frame reference.

where: T_c : constant component, T_{per} is the amplitude of the load torque oscillation, and $\omega_{per} = 2\pi f_{per}$.

The motor speed can be obtained from the torque using this mathematical expression:

$$\sum T(t) = T_{motor}(t) - T_{load}(t) = J \frac{d\omega_r}{dt} \quad (2)$$

$$\omega_r = \frac{1}{J} \int_t (T_{motor}(\tau) - T_{load}(\tau)) d\tau \quad (3)$$

The motor torque is equal to the T_c : constant part of the load expression in the steady state. As a result, the rotor velocity ω_r is expressed by:

$$\omega_r = -\frac{1}{J} \int_t (T_c \cos(\omega_c \tau)) d\tau + C = -\frac{T_c}{J\omega_c} \sin(\omega_c t) + \omega_{r0} \quad (4)$$

So, the mechanical rotor position is given by the integration of the mechanical speed:

$$\theta_r(t) = \int_0^t \omega_r(\tau) d\tau = -\frac{T_c}{J\omega_c^2} \cos(\omega_c t) + \omega_{r0} t \quad (5)$$

For a healthy motor in ideal operating conditions $\theta_r(t) = \omega_{r0} t$, consider the integration constant zero. The mechanical rotor position θ_r oscillations have an effect on the rotor MMF. The rotor MMF in the rotor reference frame (R), which is treated as a wave with p pole pairs and a frequency $s f_{st}$, is expressed by:

$$F_{rt}^{(R)}(\theta', t) = F_{rt} \cos(p\theta' - s\omega_s t) \quad (6)$$

where: $\theta = \theta' + \theta_r$ as seen in Figure 4.

$$\theta' = \theta - \omega_{r0} t - \frac{T_c}{J\omega_c^2} \cos(\omega_c t) \quad (7)$$

Using the expression $\omega_{r0} = \frac{1-s}{p} \omega_{st}$, the rotor MMF may be translated to the stationary stator reference frame as:

$$F_{rt}^{(R)}(\theta, t) = F_{rt} \cos(p\theta - \omega_{st} t - \beta \cos(\omega_{per} t)) \quad (8)$$

where: $\beta = p \frac{T_{per}}{J\omega_{per}^2}$.

As seen in equation (8), $\beta \cos(\omega_{per} t)$ characterizes the phase modulation in the phase of the MMF wave. The reason causing the oscillation of the torque has no direct impact on the MMF of the stator. Therefore, it can be written as follows:

$$F_{st}(\theta, t) = F_{st} \cos(p\theta - \omega_s t - \varphi_s) \quad (9)$$

We define the air gap flux density, $B(\theta, t)$ as the total MMF multiplied by the permeance Λ (which is considered a constant for the sake of simplicity:

$$\begin{aligned} B(\theta, t) &= (F_{st}(\theta, t) + F_{rt}(\theta, t))\Lambda \\ &= B_s \cos(p\theta - \omega_{st} t - \varphi_s) \\ &\quad + B_r \cos(p\theta - \omega_{st} t - \beta \cos(\omega_{per} t)) \end{aligned} \quad (10)$$

There is a phase modulation of the flux density $B(\theta, t)$ for the flux $\Phi(t)$. $\Phi(t)$ is calculated by performing a simple integration of $B(\theta, t)$ regarding the winding structure, which has no effect on the frequencies of the flux harmonic components, just on their amplitudes. As a result, $\Phi(t)$ is an arbitrary phase that may be stated in the following way:

$$\phi(t) = \phi_s \cos(\omega_s t + \varphi_s) + \phi_r \cos(\omega_s t + \beta \cos(\omega_c t)) \quad (11)$$

Moreover, the relationship between the current and the magnetic flux is given by Farady law as follows:

$$V(t) = R_s I(t) + \frac{d\phi(t)}{dt} \quad (12)$$

with $V(t)$ is the voltage introduced from the source.

The derivation of the flux from (11) yields:

$$\begin{aligned} \frac{d\phi(t)}{dt} &= -\omega_{st} \phi_s \sin(\omega_s t + \varphi_s) - \omega_{st} \phi_r \sin(\omega_{st} t \\ &\quad + \beta \cos(\omega_{per} t)) + \omega_{per} \beta \phi_r \sin(\omega_{st} t \\ &\quad + \beta \cos(\omega_{per} t)) \sin(\omega_{st} t) \end{aligned} \quad (13)$$

Finally, the stator current in any selected phase will be given by the expression below:

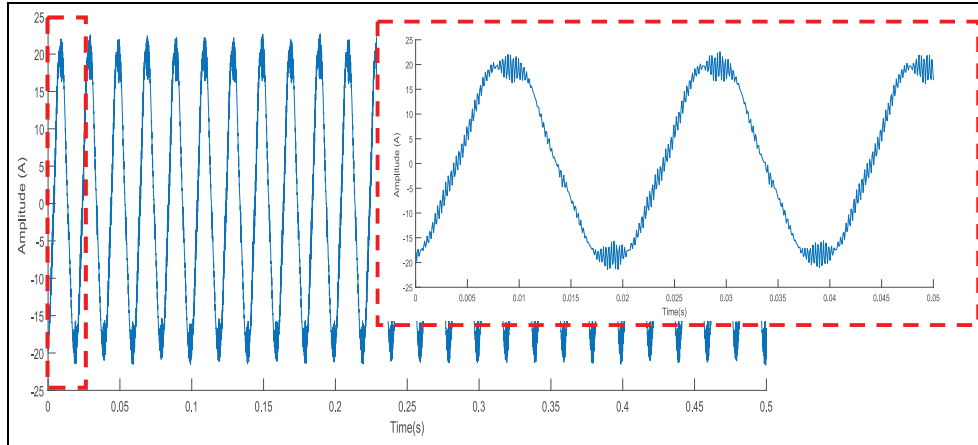


Figure 5. The current signal in the time domain.

$$I(t) = \frac{1}{R_{st}} \left(V(t) - \frac{d\phi(t)}{dt} \right) \quad (14)$$

$$I(t) = \frac{1}{R_s} \left(V(t) - \left[-\omega_s \phi_s \sin(\omega_s t + \varphi_s) + \sin(\omega_s t + \beta \cos(\omega_{per} t)) \right] \left[-\omega_s \phi_r + \omega_{per} \beta \phi_r \sin(\omega_s t) \right] \right) \quad (15)$$

In the work presented by Feng et al.,²⁷ the gear fault generates a load torque oscillation that produces both FM (Frequency Modulation) and AM (Amplitude Modulation) effects on the stator current, with the supply frequency as a carrier frequency. The FM and AM frequencies are equal to the key frequencies of the gearboxes (meshing frequency, rotating frequency, and default frequency in the case of defective gears).

The current is expressed, finally, as follows:

$$I(t) = i_{st}(t) + i_{rt}(t) = I_{st} \sin(\omega_s t + \varphi_s) + I_{rt} \sin(\omega_s t + \beta \cos(\omega_{per} t)) \quad (16)$$

With: $i_{st}(t)$ is the result from the stator MMF, which is unaffected by the torque variation and the $i_{rt}(t)$, a direct result of the rotor MMF, is the term used to describe the phase modulation caused by torque variability. Feng et al. used this demonstration that explains the impact of the torque fluctuation on the stator current to describe the electro-mechanical interaction between the motors and the mechanical systems.

Experimental study

The objective beyond this work is to study the impact of a tooth defect in the planetary gearbox on the current signature. Therefore, we started by analyzing the motor current signal under different operating conditions. The first step was to independently investigate the state of the motor before its connection to the mechanical system. Later, the electrical signal of the

motor will be presented for the healthy configuration and in the presence of a tooth defect. Finally, in order

to validate the results, the current signal will be compared with the vibration and the acoustic radiation signals.

Free motor state investigation

Figure 5 presents the phase current signal's time domain evolution. The electrical fundamental period is dominant.

In the ideal case, the current measured in one phase should be perfectly sinusoidal. Therefore, it presents a lot of imperfections, which can be related to the sector or the power supply.²⁸ Figure 6 illustrates the frequency spectrum for free motor, showing the fundamental frequency at 50 Hz.

Besides the fundamental frequency, we notice the presence of the harmonics (second, third, fourth, and fifth). These harmonics are not always related to a probable motor fault but also to variations in motor load, inertia, torque, supply voltage, or speed oscillation of the motor.²⁹

Within the same context, besides the supply frequency and its harmonics, the current spectrum in Figure 6 shows additional frequencies with important amplitudes. Although the motor is, theoretically, supposed to be well built, its assembly is impossible without getting a minimum residual eccentricity. In addition, the process of aligning the motor and load will never be perfect. Hence, additional forces will appear increasing the eccentricity of the rotor. On the other hand, the state of wear and the characteristics of the bearing seat will also influence the position of the rotor within the static housing. The combination of all these phenomena will lead to mate eccentricity,

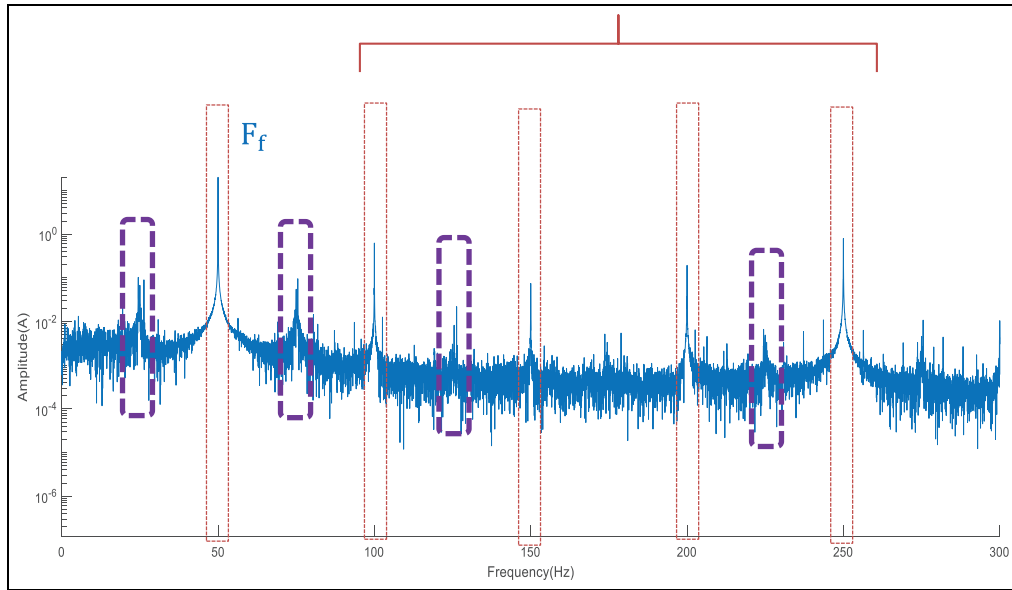


Figure 6. The frequency spectrum of the free motor's current signal.

which involves static and dynamic eccentricity. The coexistence of static and dynamic eccentricity will give rise to harmonics (25.5 and 74.5 Hz) given by the equation (17) for $n = 1$, even in healthy motors.³⁰

$$f_{\text{ecc}} = F_f \pm nF_r \quad (17)$$

where $n = 1, 2, 3, \dots$

The rotor may be regarded healthy if the amplitude of these harmonics is more than 50 dB less than the amplitude of the fundamental frequency component.³¹

The impact of the planetary gearbox on measurements

The mechanical system described in section.2 is connected to the motor. The impact of the gearboxes on the spectra of the current signal is shown in Figure 7. The results are plotted for the free motor (in blue) and for the current after connecting the motor to the test bench (in red).

The comparison between the current signals confirms the presence of additional peaks, which correspond to key frequencies of the planetary gearboxes. The existence of mechanical frequencies in the motor current signal is seen as a modulation of the supply frequency (given 50 Hz). Figure 7(b) shows components related to gear meshing frequency: $|F_f \pm F_{\text{gm}}|$. Likewise, Figure 7(c) shows sidebands around the fundamental frequency, which confirm the influence of each mechanical component. The fact that carrier frequency and its harmonics have noticeable amplitude at: $|F_f \pm nF_c|$, $n \in \mathbb{N}$ is explained by the effect of carrier gravity as detailed in Hammami et al.³² Also, the movements of sun are transmitted through the input shaft to the motor, affecting the current signal

as well. This is well observed by the presence of sun related frequencies: $F_f \pm F_s$. Hence, we notice the presence of a relative planet frequency $F_f \pm F_{\text{pc}}$ with an important amplitude. In fact, the presence of this frequency is probably related to some mounting problems on one of the planets. These frequencies are confirmed by vibrational signals obtained simultaneously while measuring the current signals.

In the following sections, the current signal results will be compared to those of vibration and acoustic pressure for different case studies.

The effect of the planet's fault on measurement

Time domain. In this section, we are studying the effect of the groove introduced on one of the planets on different measured signals, as shown in Section 2.4. Figure 8 illustrates the current, vibration and acoustic pressure signals for this defect. The impact of the presence of this defect can be observed with different degrees of clarity for the three signals.

Introducing the planet defect has impacted the vibration signals and the acoustic pressure, as illustrated in Figure 8(c) for the time signal by the periodic increase of the amplitude. However, the impact of the planet defect on the current time signal, as shown in Figure 8(a), is barely visible. Therefore, in order to go deeper in the investigations and check the frequency content of the signals, spectra are studied.

Frequency domain. Figure 9 depicts a comparison between two spectra of current time signals shown in the last section for the healthy and defected cases to highlight the impact of the planet tooth defect on the current signal.

The pitting included on the planet has affected the current signals by increasing the amplitude of some

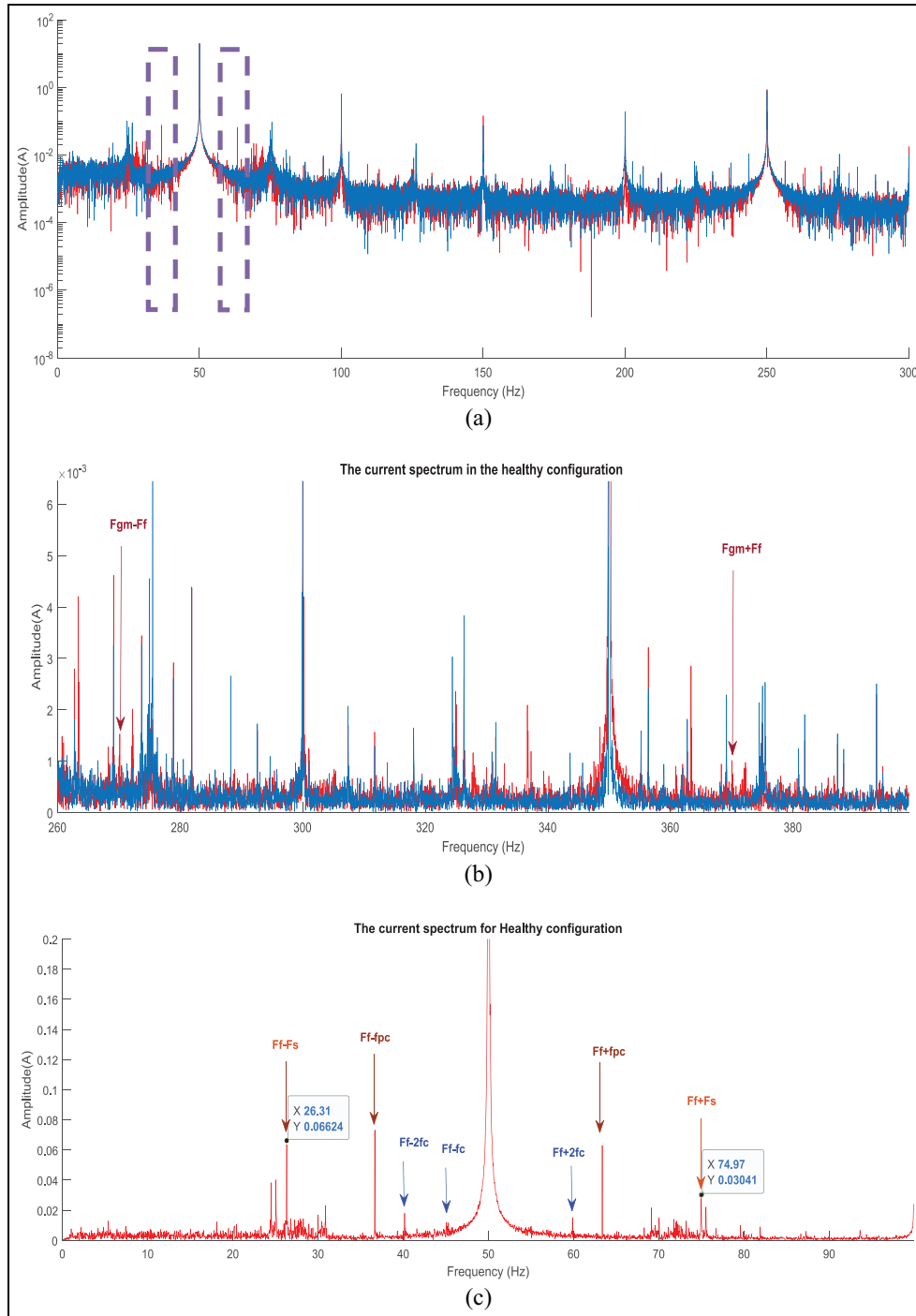


Figure 7. The current signal (blue: for free motor, red: the motor is already connected to the planetary gearbox): (a) zoom in frequency range [0 Hz; 300 Hz], (b) zoom in frequency range [260 Hz; 400 Hz], and (c) current signal in the presence of defect [0 Hz; 100 Hz].

frequency components in addition to other frequencies that emerge. The changes in the amplitude of some frequencies, such as the components related to sun frequency ($F_r \pm F_s$) after including the pitting are more consistent in MCSA. Furthermore, we notice additional frequencies, as seen in Table 3, due to the presence of tooth defects located at: $|F_r \pm nF_c \pm pF_{dp}|$ where: ($p = 0$ and $n = 1, 3, 4$ or; $p = 1$ and $n = 1$ or; $n = 0$ and $p = 2$). This influence impacts the

movement of the carrier, which explains the emergence of the frequencies related to the carrier and its harmonics in the current spectrum (Figure 9).

Figure 10 shows the impact of pitting on both the vibration and acoustic pressure by comparing the signals in the healthy configuration and in the presence of a planet defect. Figure 10(b) illustrates the appearance of the pitting frequency ($F_{dp} = 13.35$ Hz). The figure highlights that the impact of the pitting on the

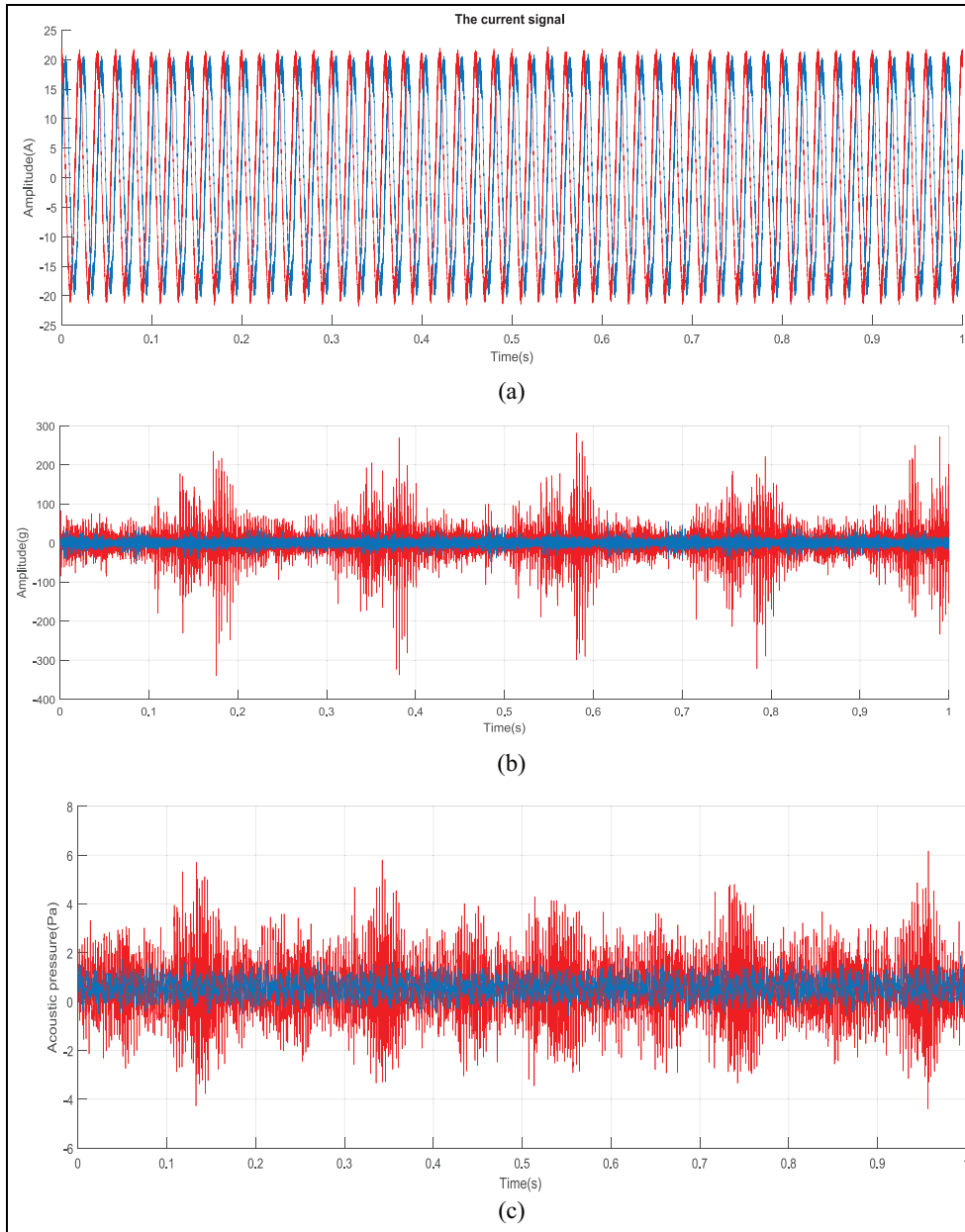


Figure 8. Temporal signal of the measurements (Red: Signal in the presence of defect; Blue: Healthy configuration): (a) the current signal, (b) the vibration signal of the test gearbox, and (c) the acoustic pressure.

vibration is more significant ($5 \text{ times } 5 \cdot 10^{-3}$) than the impact recorded by the microphones ($5 \cdot 10^{-3}$). This contrast is inversely explained by the distance separating the accelerometer and the microphones from the defected gear. Literally, this distance impacts the attenuation of the defect's signature, and as a consequence, the amplitude of its frequency in the frequency spectra.

In Figure 11, the spectrum shows that not only the defect frequency is pointed up by the planet pitting, but also drawn attention to the appearance of the carrier frequency and its harmonics (nF_c , $n = \{1, 2, 3, \dots\}$). The appearance of the carrier frequencies and their harmonics on the experimental spectra is connected to

the carrier's gravity as an extra source of vibrations. Indeed, pitting excites the carrier more, implying that the accelerometer receives more force. Thus, gravity is more accentuated as a periodic excitation source in the case of a defected configuration.

However, in Figure 12 in both the vibration signals and the acoustic pressure, the impact of the planet pitting is enhanced by the appearance of other sidebands given by $|F_{gm} \pm nF_c \pm pF_{dp}|$. Finally, in the same spectra comparing between the healthy configuration and the current spectrum in the presence of the planet pitting, we notice the increase of the amplitude related to the carrier frequency $mF_{gm} \pm nF_c$ (i.e.: 921 Hz, 931 Hz..).

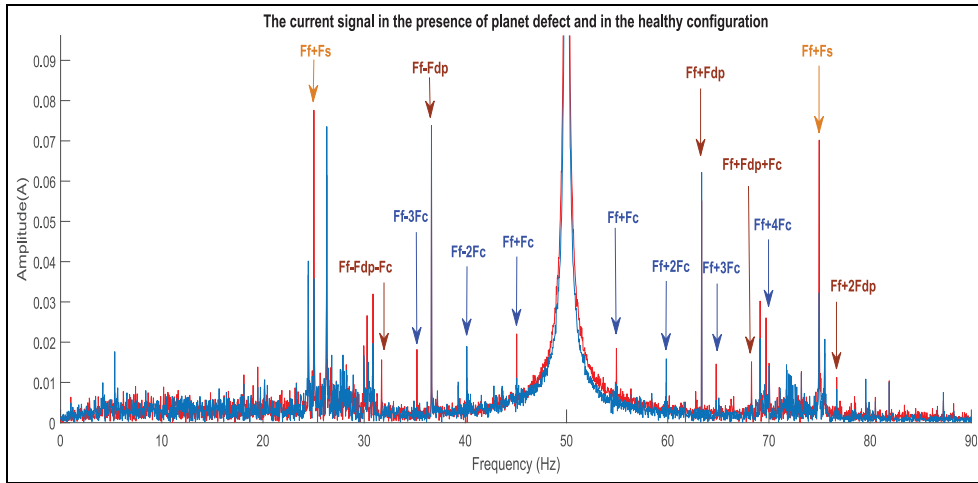


Figure 9. The current spectrum in the presence of the planet defect (Red: Defected configuration; Blue: Healthy configuration).

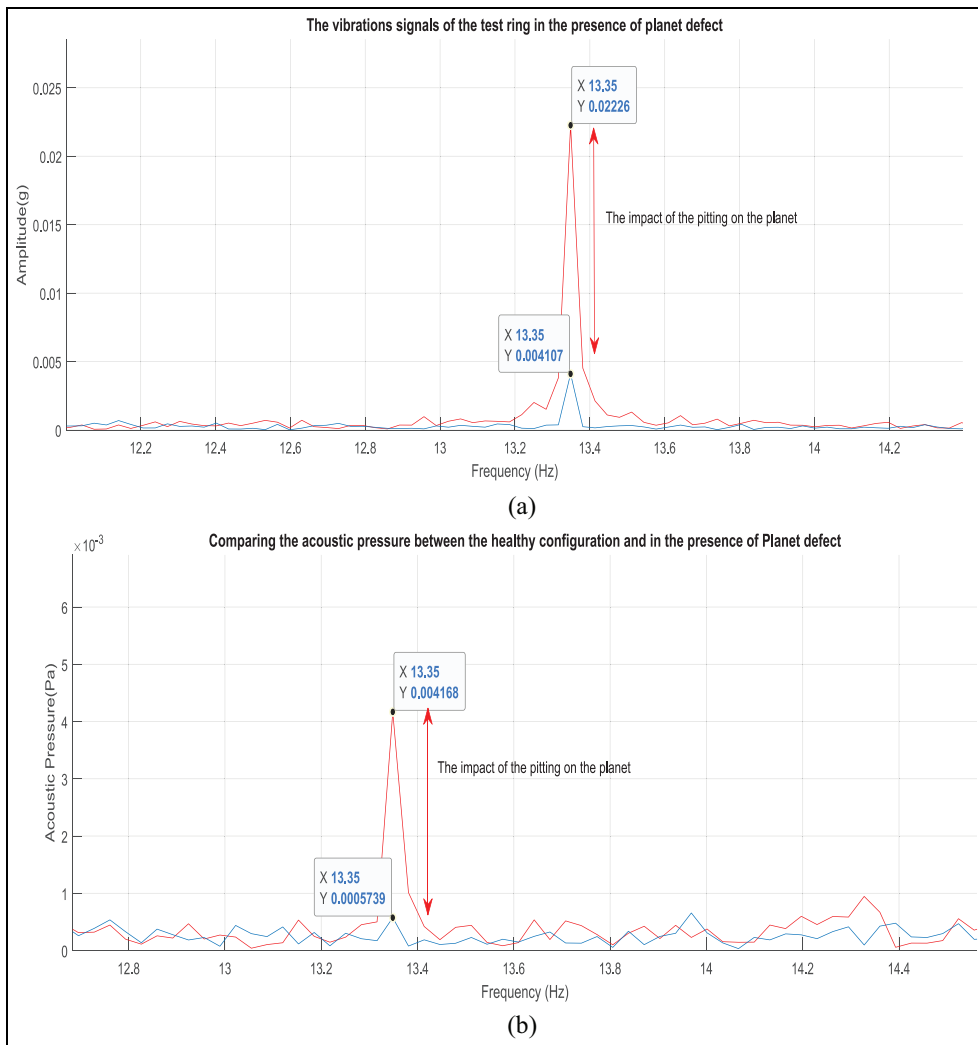


Figure 10. Planet defect identification by vibration (a) and acoustic pressure (b).

Table 3. Frequencies (Hz) for each combination of the expression.

n \ p	0		1		2		3		4	
	-	+	-	+	-	+	-	+	-	+
0			45.07	54.93	40.14	59.86	35.22	64.78		69.71
1	-		31.72							
2	+	76.7		68.28						

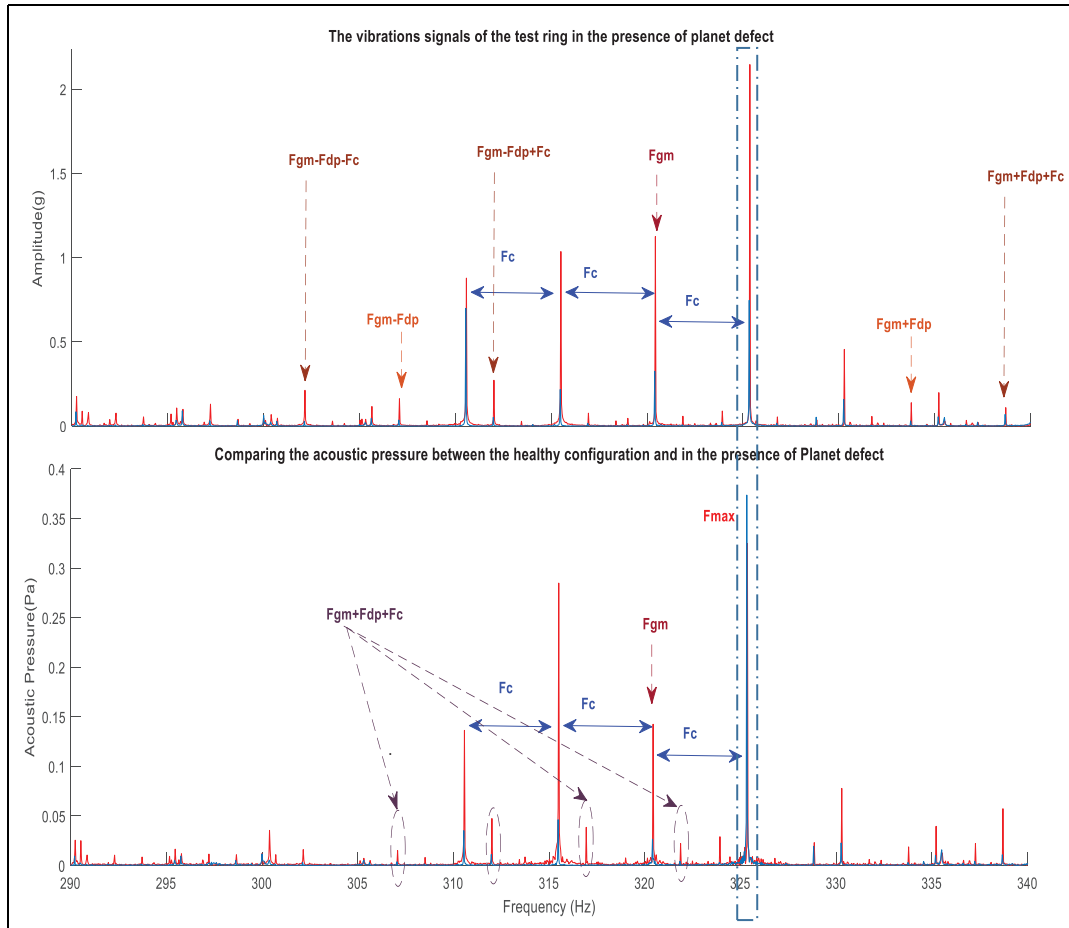


Figure 11. The vibration spectrum in the presence of planet defect comparing the acoustic pressure recorded in both configuration healthy and in the presence of planet pitting.

Combined defects in the test gearbox

In this section, two types of defects are introduced simultaneously (crack on one tooth of the sun gear and pitting on one tooth of the planets). Figure 13 presents the current spectrum in different configurations of the gears. The current signal illustrated in Figure 13 investigates the impact of the type, placement, and dimensions of the defect on the motor current.

In Figure 13, four configurations are presented: (1) The reference plots, which correspond to a healthy set of gears; (2) The spectra in the presence of a defected planet; (3) The spectra in the presence of a sun crack;

and finally, (4) The current frequency spectrum with both defects.

The current spectrum in green is recorded in the presence of the sun pitting, considered a local defect. An impulse signal modulates the vibration signal when the local fault meshes with one of the planet gears. As a result, when the local fault exits the meshing area, the vibration signal returns to normal. However, the impact of the vibrations accrued from the sun pitting is observed in the current spectrum by the related characteristic frequency $F_f + F_{ds}$ (110 Hz). When the sun has a local defect, it meshes with the

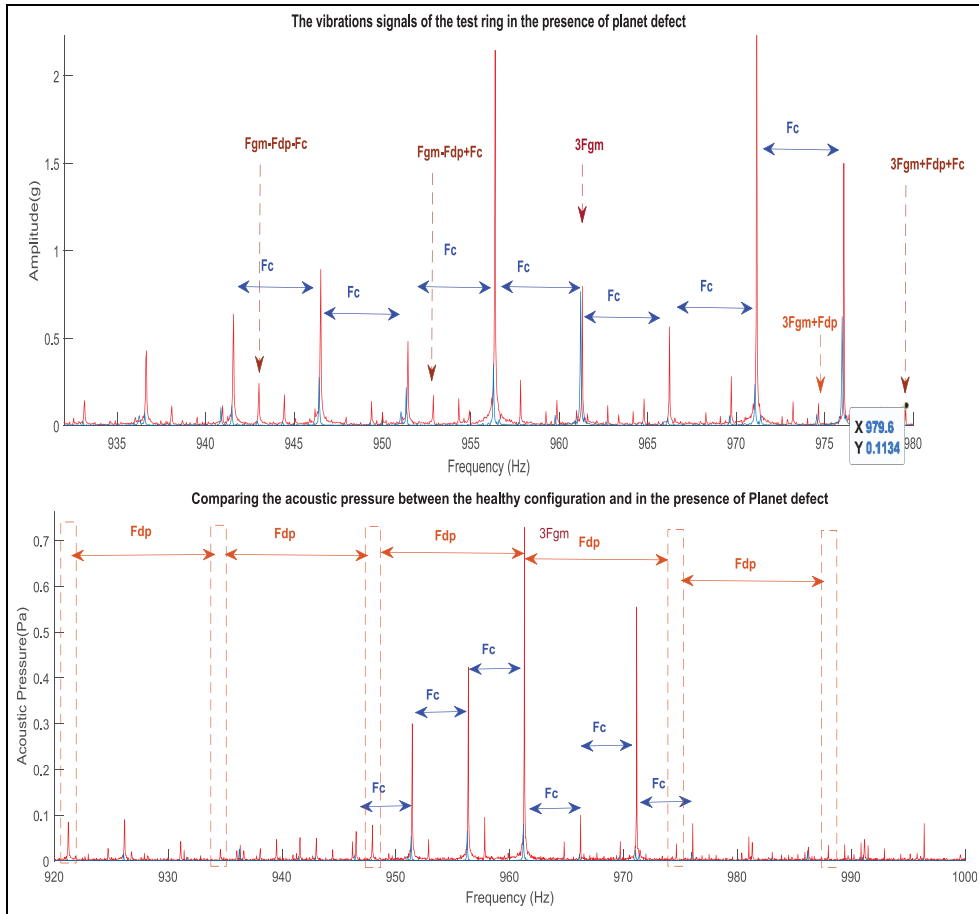


Figure 12. The vibration spectrum in the presence of planet defect comparing the acoustic pressure in the presence of planet pitting in high frequency.

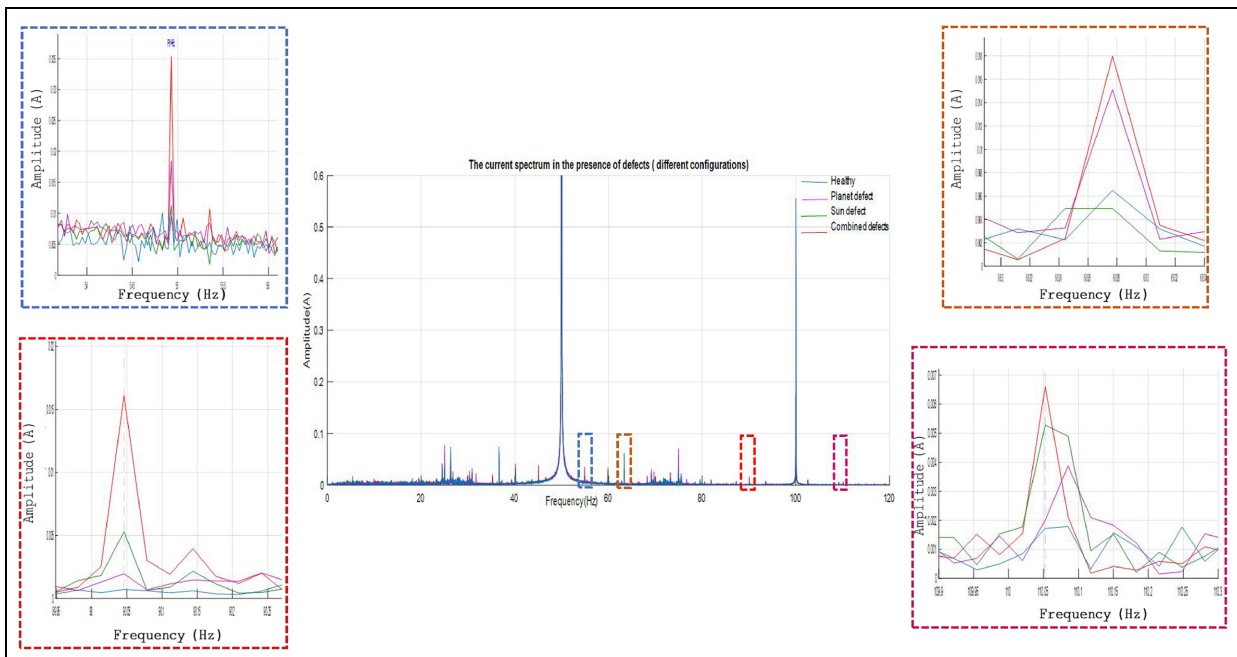


Figure 13. The current spectrum in the presence of combined defect.

three planets therefore, its appearance in the current spectrum is enhanced each time the rotating sun frequency is relative to the carrier $F_F + F_{sc} - F_{ds}$ (example: 80 Hz)

In the same figure, the spectrum presents the impact of the co-existing of the sun pitting and the planet defect on the current signal. In addition, the presented results demonstrate that the presence of both defects enhances the amplitude of the related frequencies of each defect, as demonstrated above. The amplitude of the peak increases as the carrier frequency increases $F_f + F_c$ (Figure 13). This frequency can be explained by the contact between both defects, which can generate an additional source of vibration and impact the spectra accordingly.

Conclusion

Using Motor Current Signature Analysis (MCSA), this article provided a thorough examination of the effect of tooth defects on stator current by developing an analytical correlation between the motor current signal and any torque perturbations. This explanation was followed by experimental measurements of different physical signals. The main results illustrated the impact of different types of tooth defects on the motor current signals. The perturbations resulted from the gear defects in the test planetary gearbox impacting the phase current signature. This impact is seen in Frequency Modulation (FM) and Amplitude Modulation (AM). The temporal signal of the phase current did not highlight the influence of the mechanical system neither the gears defects. Therefore, a frequency spectrum is presented using the Fast Fourier Transform. Fortunately, the gear defects are seen in the current spectrum as additional peaks in lateral sidebands around the supply frequency. The results obtained in the current signature were justified by the vibration signals and the acoustic pressure to highlight the sensitivity of the approach and justify the efficiency of the motor current signal analysis in defect detection. The proposed method has proven its effectiveness against the acoustic emission and vibration method. Indeed, the approaches studied in this paper are sufficiently sensitive to gear defects. Regarding the implementation of the control devices, it is better to use more microphones in different directions and in optimal arrangements. The MCSA is effective and easy to implement, but its effectiveness needs to be tested, taking into account the presence of electro-mechanical faults and their correlations. The electrical model will be extended in the future, increasing its complexity to be closer to the real system by introducing defects in the electric machine. Because of its accuracy and, more importantly, its accessibility under various operating situations, this methodology would be a leading way to diagnose the rotating system.

Acknowledgements

We would like to express our gratitude to the University of Cantabria collaboration project for providing PhD training to Sfax University students.

Declaration of conflicting interests

The author(s) declared no potential conflicts of interest with respect to the research, authorship, and/or publication of this article.

Funding

The author(s) disclosed receipt of the following financial support for the research, authorship, and/or publication of this article: The authors would like also to acknowledge Project PID2020-116213RB-I00 funded by the Ministry of Science and Innovation.

ORCID iD

Mohamed Amine Ben Souf  <https://orcid.org/0000-0001-7271-5660>

References

1. Chaari F, Zimroz R, Bartelmus W, et al. Modeling of local damages in spur gears and effects on dynamics response in presence of varying load conditions. *Proc Survell* 2011; 6: 1–19.
2. Rincon AFD, Viadero F, Iglesias M, et al. Effect of cracks and pitting defects on gear meshing. *Proc IMechE, Part C: J Mechanical Engineering Science* 2012; 226(11): 2805–2815.
3. Inturi V, Penumakala PK and Sabareesh GR. Effect of multiple defects and multi-component failure on the dynamic behaviour of a wind turbine gearbox. *Arab J Sci Eng* 2022; 47: 8969–8983.
4. Inturi V, Penumakala PK and Sabareesh GR. Detection of local gear tooth defects on a multistage gearbox operating under fluctuating speeds using DWT and EMD analysis. *Arab J Sci Eng* 2021; 46: 11999–12008.
5. Al-Shyyab A and Kahraman A. A non-linear dynamic model for planetary gear sets. *Proc IMechE, Part K: J Multi-body Dynamics* 2007; 221(4): 567–576.
6. Inalpolat M and Kahraman A. A theoretical and experimental investigation of modulation sidebands of planetary gear sets. *J Sound Vib* 2009; 323(3-5): 677–696.
7. Zimroz R and Bartkowiak A. Investigation on spectral structure of gearbox vibration signals by principal component analysis for condition monitoring purposes. *J Phys Conf Ser* 2011; 305: 012075.
8. Miao Q and Zhou Q. Planetary gearbox vibration signal characteristics analysis and fault diagnosis. *Shock Vib* 2015; 2015. 8, Article ID 126489.
9. Yi Y, Qin D and Liu C. Investigation of electromechanical coupling vibration characteristics of an electric drive multistage gear system. *Mech Mach Theory* 2018; 121: 446–459.
10. Balan H, Buzdugan MI and Karaisas P. Fault identification on electrical machines based on experimental analysis. In: *Advances in condition monitoring of machinery in non-stationary operations*. Springer Heidelberg, 2014, pp.611–630.

11. Feki N, Clerc G and Vex P. An integrated electro-mechanical model of motor-gear units—Applications to tooth fault detection by electric measurements. *Mech Syst Signal Process* 2012; 29: 377–390.
12. Ottewill JR, Ruszczak A and Broda D. Monitoring tooth profile faults in epicyclic gearboxes using synchronously averaged motor currents: Mathematical modeling and experimental validation. *Mech Syst Signal Process* 2017; 84: 78–99.
13. Kia SH, Henao H and Capolino G-A. Gearbox monitoring using induction machine stator current analysis. In: *2007 IEEE international symposium on diagnostics for electric machines, power electronics and drives, 2007*, pp.149–154. New York, NY: IEEE.
14. Kia SH, Henao H and Capolino GA. Analytical and experimental study of gearbox mechanical effect on the induction machine stator current signature. *IEEE Trans Ind Appl* 2009; 45(4): 1405–1415.
15. Zhou Z, Chen Z, Spiriyagin M, et al. Dynamic response feature of electromechanical coupled drive subsystem in a locomotive excited by wheel flat. *Eng Failure Anal* 2021; 122: 105248.
16. Gao A, Feng Z and Liang M. Permanent magnet synchronous generator stator current AM-FM model and joint signature analysis for planetary gearbox fault diagnosis. *Mech Syst Signal Process* 2021; 149: 107331.
17. Henao H, Kia SH and Capolino GA. Torsional-vibration assessment and gear-fault diagnosis in railway traction system. *IRE Trans Ind Electron* 2011; 58(5): 1707–1717.
18. Yacamini R, Smith KS and Ran L. Monitoring torsional vibrations of electro-mechanical systems using stator currents. *J Vib Acoust* 1998; 120(1): 72–79.
19. Abbes MS, Bouaziz S, Chaari F, et al. An acoustic-structural interaction modelling for the evaluation of a gearbox-radiated noise. *Int J Mech Sci* 2008; 50(3): 569–577.
20. Amarnath M and Praveen Krishna IR. Empirical mode decomposition of acoustic signals for diagnosis of faults in gears and rolling element bearings. *IET Sci Meas Technol* 2012; 6(4): 279–287.
21. Baydar N and Ball A. A comparative study of acoustic and vibration signals in detection of gear failures using Wigner–Ville distribution. *Mech Syst Signal Process* 2001; 15(6): 1091–1107.
22. Boudhraa S. *Multidomain model and condition monitoring of gears transmission*. PhD thesis, National Engineering School of Sfax and University of Cantabria, 2022.
23. Hammami A, Fernandez Del Rincon A, Chaari F, et al. Effects of variable loading conditions on the dynamic behaviour of planetary gear with power recirculation. *Measurement* 2016; 94: 306–315.
24. Fan L, Wang S, Wang X, et al. Nonlinear dynamic modeling of a helicopter planetary gear train for carrier plate crack fault diagnosis. *Chin J Aeronaut* 2016; 29(3): 675–687.
25. Chen K, Hu J and Peng Z. Analytical framework of gearbox monitoring based on the electro-mechanical coupling mechanism. *Energy Proc* 2017; 105: 3138–3145.
26. Blodt M, Chabert M, Regnier J, et al. Mechanical load fault detection in induction motors by stator current time-frequency analysis. *IEEE Trans Ind Appl* 2006; 42(6): 1454–1463.
27. Feng Z, Chen X and Zuo MJ. Induction motor stator current AM-FM model and demodulation analysis for planetary gearbox fault diagnosis. *IEEE Trans Ind Inform* 2019; 15(4): 2386–2394.
28. Miljković D. Brief review of motor current signature analysis. *HDKBR Info Mag* 2015; 5(1): 14–26.
29. Karmakar S, Chattopadhyay S, Mitra M, et al. (*Power Systems*), *Induction Motor Fault diagnosis, approach through current signature analysis*. Singapore: Springer, 2016.
30. Cabanas MF, Melero MG, Orcago GA, et al. *Técnicas para el mantenimiento y diagnóstico de máquinas eléctricas rotativas*. 1998.
31. Hirvonen R. On-line condition monitoring of defects in squirrel cage motors. In: *Proceedings of the 1994 international conference on electrical machines*, Paris, France, vol. 2, pp.267–272. New York, NY: IEEE.
32. Hammami A, Del Rincon AF, Rueda FV, et al. Modal analysis of back-to-back planetary gear: experiments and correlation against lumped-parameter model. *J Theor Appl Mech* 2015; 53(1): 125–138.

Appendix

Abbreviations

F_f	Fundamental supply frequency
S	Sun
R	Ring
P	Planet
N	Rotational speed
Z_i (i = s,r,p)	Teeth number resp. to the sun, ring and planet
F	Frequency
R_{sp}	The sun-planet gear ratio
R_{sc}	Transmission ratio
F_s	Sun frequency
F_c	Carrier frequency
F_{pp}	Planet passing
F_p	Planet frequency
F_{sc}	Sun frequency with respect to the carrier
F_{pc}	Planet frequency with respect to the carrier
F_{gm}	Meshing frequency
T_{per}	Amplitude of the load perturbation
ω_{per}	The velocity of the load of perturbation introduced
T	Torque load
ω_r	Rotor velocity
p	Number of pairs of poles
S	Motor slip
Rt	Rotor
St	Stator
B	Air gap flux density
I	Current
F_{rt}	Rotor frequency
F_r	Rotational frequency
f_{per}	The frequency of mechanical perturbation
F_{dp}	The defected planet frequency
F_{ds}	The defected sun frequency
